

Universal Drag Force Scaling in High Stokes Number Oscillatory Flows of He II

M. J. Jackson,¹ D. Schmoranzner,¹ L. Doležal,¹ Š. Midlik,¹ T. Skokánková,¹ M. Skyba,² J. Bahyl,³ and L. Skrbek³

¹*Faculty of Mathematics and Physics, Charles University,
Ke Karlovu 3, 121 16, Prague 2, Czech Republic.*

²*Institute of Physics ASCR, v.v.i., Na Slovance 2, 182 21, Prague 8, Czech Republic.*

³*Faculty of Mathematics, Physics and Informatics,
Comenius University, Mlynská dolina F1, Bratislava, Slovak Republic.*

We present a unified analysis of the drag forces acting on oscillating bodies submerged in superfluid ^4He - He II: vibrating wire resonator, tuning fork, double-paddle, and torsionally oscillating disc. We find that in the two-fluid temperature range above 1 K, for high Stokes number oscillatory flows, the drag forces originating from the normal component of He II, described in terms of suitable dimensionless parameters, exhibit a clearly defined universal scaling behavior, derived by modification of classical fluid dynamical laws and verified in classical fluids. We use this approach to illustrate the transition from laminar to turbulent drag regime in He II oscillatory flows and compare the critical velocities associated to the production of quantized vorticity in the superfluid component with the critical velocities for the first flow instabilities occurring in the normal component. We show that, depending on the temperature and geometry of the flow, either type of instability may occur first and we demonstrate a crossover caused by temperature dependence of the kinematic viscosity of the normal fluid. Additionally, we develop a formalism describing the ballistic phonon gas at $T < 0.6$ K, allowing direct comparison between measurements with various resonators in He II and NEMS in classical dilute gases. We verify that the relativistic gas of phonons – quasiparticles with zero rest mass – shows the same asymptotic behavior as classical gases and confirm the universality scaling relation for high frequency flows proposed by Ekinici *et al.* [*Lab Chip* **10**, 3013 (2010)].

March 21, 2018

I. PREFACE

Historically, experiments on oscillatory flows of classical viscous fluids have been studied since the days of G. G. Stokes², with many notable developments made in the last century^{3–6}. In the modern era, oscillating flows have gained notoriety thanks to developments in micro- and nanomechanical engineering, where access to MEMS/NEMS devices has offered unprecedented sensitivity and resolution in fluid dynamical experiments, allowing the transition from continuum to the ballistic (kinetic) regime to be probed at easily attainable pressures, formulate universality relations^{1,7,8} and directly probe fluid boundary layers⁹.

An extremely broad range of working fluids of known physical properties^{10–12} may be obtained when traversing the different phases of helium, even limiting ourselves to the common isotope ^4He . The normal fluid phase of ^4He - He I is a very interesting working fluid thanks to its extremely low kinematic viscosity, ν , which provides very high Reynolds number ($\text{Re} \approx 10^7$) flows in controlled laboratory experiments^{13,14}. Similarly, cryogenic He gas provides extremely large Rayleigh numbers ($\text{Ra} \approx 10^{17}$) in buoyancy driven flows such as Rayleigh-Bénard convection¹⁵. Normal liquid ^4He , known as He I, undergoes a second-order superfluid transition at $T_\lambda \approx 2.17$ K. Superfluid ^4He - He II – is a quantum fluid, and its flow properties cannot be described by means of classical fluid dynamics. According to Landau's two-fluid model^{16,17}, it behaves as if composed of two inter-penetrating liquids – the normal and superfluid components – with corresponding velocity fields and temperature-dependent densities.

At the superfluid transition at T_λ , the density of the normal component accounts for 100% of the total density, but drops rapidly with decreasing temperature and vanishes for $T \rightarrow 0$ K.

While the normal fluid behaves classically, possessing finite viscosity and carrying the entire entropy content of He II, the superfluid component has neither entropy nor viscosity and, due to quantum restrictions, the vorticity is constrained into line singularities called quantized vortices. Quantum turbulence¹⁸ therefore takes the form of a tangle of quantized vortices in the superfluid component which typically coexist with classical-like turbulent flow of the normal fluid above $\simeq 1$ K, where appreciable amount of normal fluid exists. In the presence of quantized vortices, the otherwise independent normal and superfluid velocity fields become coupled by the mutual friction force which arises due to quasiparticles scattering off the cores of quantized vortices.

At temperatures below $\simeq 1$ K, a transition to a non-Newtonian ballistic regime occurs in the normal component of He II, in a similar fashion as observed in dilute classical gases. We develop a formalism based on the theory of ideal Bose gases which allows direct comparison between experiments performed in the ballistic regime of the superfluid below $\simeq 0.6$ K and in dilute gases. This formalism is used to test the validity of the universal scaling laws¹ recently proposed for classical gases of massive particles, in a gas of thermal excitations (phonons) with a zero rest mass, bridging the gap between classical and quantum fluids as well as between room temperature and cryogenic experimentation. Consequently, standard cryogenic techniques such as dilution refrigeration¹⁹





could used to extend the accessible parameter space in the ballistic regime using only micromachined resonators operating at kHz frequencies and compare the results directly to those obtained in classical gases with NEMS devices resonating in the MHz range.

Oscillatory quantum flows of He II have been studied using various oscillators such as discs^{20,21}, piles of discs²², spheres^{23–25}, grids^{26–30}, tuning forks^{31–34}, reeds³⁵, double paddles^{36–38}, cylinders of rectangular³⁹ or circular cross-section (wires)^{40–43} since the discovery of superfluidity, and have lead to important insights to this fundamental physical phenomenon. For reviews, see^{44,45}. Nevertheless, a universal picture of scaling in superfluid hydrodynamics is still missing, which motivated us to investigate oscillatory quantum flows of He II due to mechanical oscillators of different geometries – a vibrating tuning fork, a microwire loop, a torsionally oscillating disc and a double paddle.

We find that for high Stokes number viscous oscillatory flows (above $\simeq 1$ K, with the viscous penetration depth in the normal fluid much smaller than the characteristic size of the oscillator), the drag forces originating from the normal component of He II are described in terms of a single dimensionless parameter and exhibit a clearly defined universal scaling behavior. We identify and compare the critical velocities related to the production of quantized vorticity in the superfluid component with the critical conditions for the instabilities occurring in the normal component. We find that either type of instability may occur first and over certain range of parameters exist on its own. We even demonstrate a crossover between the type of the first instability, caused by temperature dependence of the kinematic viscosity of the normal fluid. Either instability eventually acts as a trigger for the other one, depending on the temperature and geometry of the flow.

II. INTRODUCTION

We begin our discussion of the dynamics of superfluids with the Newtonian-like hydrodynamic description applicable above $\simeq 1$ K, as this corresponds to most of the experiments discussed here, and later introduce the ballistic, non-Newtonian description, valid at lower temperatures.

A. Superfluid Hydrodynamics

On a phenomenological level, superfluid ^4He - He II at finite temperatures is described as consisting of two components - a viscous normal component and an inviscid superfluid component¹⁶. Their temperature-dependent densities, ρ_n and ρ_s add up to the (nearly temperature independent) total density of He II, ρ . With no quantized vortices present, isothermal flows of both components have independent velocity fields, and both can

easily become turbulent. Quantum turbulence can be loosely defined as the most general way of motion of quantum fluids displaying superfluidity. Superfluid turbulence exists in the superfluid component of He II, due to quantum mechanical restriction resulting in quantized vorticity, in the form of a tangle of singly quantized vortices¹⁷, with the quantum of circulation given as $\kappa = h/m_4 \approx 0.997 \times 10^{-7} \text{ m}^2\text{s}^{-1}$, where h is the Planck constant and m_4 denotes the mass of a ^4He atom.

Does quantum turbulence always contain quantized vortices? Strictly speaking, if one takes the definition of quantum turbulence as turbulence occurring in quantum fluids displaying superfluidity and the two-fluid behavior literary, quantized vortices are not the necessary ingredient of quantum turbulence. One can imagine a two-fluid flow of He II consisting of turbulent normal flow and potential superflow. Indeed, in the hypothetical case of a macroscopic sample of He II free of quantized vortices (i.e., without mutual friction aiming to couple the two velocity fields), in an isothermal flow the normal and superfluid components move independently and instability criteria ought to be applied to them separately. In this hypothetical case quantized vortices must be nucleated intrinsically; this process requires critical velocities of order 10 m/s or higher. In practice, however, remnant vortices always exist in macroscopic samples of He II and nucleation of quantized vorticity takes place extrinsically, by stretching and reconnections of seed vortex loops. In many types of flow the critical velocity for extrinsic vortex nucleation is observed to be a few cm/s. As turbulence of the normal component may be possible even below this velocity threshold, it follows that there indeed is a possibility of having a quantum flow displaying (nearly) potential superflow together with a vortical flow of the normal component.

With no quantized vortices present, there is no mutual friction force and, according to the two-fluid model of Landau¹⁶, an isothermal flow of the normal component is described by the Navier-Stokes equations, while that of the superfluid component by the Euler equations for ideal fluids. Under these conditions, any body moving through He II at low velocity below the (generally independent) critical thresholds would experience drag forces originating from the normal component alone, while the drag forces offered by the superfluid component are zero (neglecting any drag due to surface waves and compressibility effects). In this case the superfluid component can be understood as a physical vacuum, merely re-normalizing the effective mass of the oscillating body. Therefore, to derive the scaling laws for the drag forces in the Newtonian limit, we must analyse the Navier-Stokes equations governing the motion of the normal component.

B. Classical Oscillatory Flows

To describe an oscillatory flow, the governing Navier-Stokes equations may be expressed in terms of a dimen-



sionless velocity $\mathbf{u}' = \mathbf{u}/U$, time $t' = t/T$ and positions $\mathbf{r}' = \mathbf{r}/L_i$ as:

$$\omega U \frac{\partial \mathbf{u}'}{\partial t'} + \frac{U^2}{L_1} (\mathbf{u}' \cdot \nabla' \mathbf{u}' + \nabla' p') = \frac{\nu U}{L_2^2} \Delta' \mathbf{u}', \quad (1)$$

where the characteristic length scales $L_{1,2}$ are used together with the characteristic velocity U to estimate the maximum magnitude of the respective velocity derivatives. An independent time scale is introduced, given (in the continuum limit) by the angular frequency of oscillation, ω . Generally, the choice of L_1 and L_2 depends on body geometry and flow parameters. Candidates may include the typical body size D , the surface roughness, or the Stokes boundary layer thickness (viscous penetration depth), which may be defined as $\delta = \sqrt{2\eta/(\rho\omega)}$, where η denotes the dynamic viscosity of the working fluid. If, for a given body $\delta \ll D$, one may say that the body oscillates in the high-frequency regime, which is equivalent to the high Stokes number $\text{St} = D^2/(\pi\delta^2) \gg 1$.

In the high frequency limit, depending on body geometry (especially surface roughness and the presence of sharp corners), δ or D may take the part of L_1 (related to the largest tangential velocity derivative) in the Navier-Stokes equation, but it is always δ that takes the part of L_2 (related to the largest velocity derivative in any direction). When the surface roughness exceeds δ , one may safely put $L_1 = L_2 = \delta$, and the Navier-Stokes equation may be expressed using only one dimensionless parameter, the boundary layer-based Reynolds number: $\text{Re}_\delta \equiv (\delta\rho U)/\eta$. Conversely, for a hydrodynamically smooth body (δ exceeds the surface roughness) without any sharp corners, such as a cylinder, we would obtain the Navier-Stokes equation with the Keulegan-Carpenter number $\text{Kc} = UT/D$ as the only relevant dimensionless parameter, as expected³.

C. Oscillatory Flows of He II

Assuming two independent velocity fields in He II, the above considerations are fully applicable for the oscillatory viscous flow of the normal component. We therefore replace ρ by ρ_n , decompose the pressure into partial pressures of the normal and superfluid components in the ratio of their respective densities, and replace δ by $\delta_n = \sqrt{2\eta/(\rho_n\omega)}$, where η denotes the dynamic viscosity of He II. Again, if, for a given body $\delta_n \ll D$, one may say that the body oscillates in the high-frequency, or high Stokes number regime $\text{St}_n = D^2/(\pi\delta_n^2) \gg 1$. Again, if the surface roughness exceeds δ_n (typically or order $1 \mu\text{m}$ in our experiments), we may put $L_1 = L_2 = \delta_n$, and the Navier-Stokes equation may be written using only one dimensionless parameter: $\text{Dn} \equiv (\delta_n\rho_n U)/\eta$, which we call the Donnelly number, in memory and honor of Russell J. Donnelly of the University of Oregon, who for the first time suggested using this dimensionless parameter, a “Reynolds number” based on the viscous penetration

depth defined for the normal component of He II only, in his joint publication with A. C. Hollis-Hallett in 1958²¹ (note that such an analysis was not included in previous work of Hollis-Hallett on the subject²⁰):

$$2 \frac{\partial \mathbf{u}'}{\partial t'} + \text{Dn} (\mathbf{u}' \cdot \nabla' \mathbf{u}' + \nabla' p'_n) = \Delta' \mathbf{u}'. \quad (2)$$

If $\delta_n \ll D$ is satisfied, and no turbulence (neither in the superfluid nor the normal component) is produced, the flow of the superfluid component will be potential and the normal component will exhibit laminar viscous flow inside the boundary layer, remaining nearly potential outside. If the typical curvature of the body is of order $1/D$, then on the scale of δ_n , its surface may be described as consisting of many planar elements. In that case, the magnitude of the dissipative component of the drag force acting on a surface element of the body is given as:

$$dF = \eta \frac{du_t}{dr_n} dS \approx \alpha \eta u_L / \delta_n dS = \alpha u_L \sqrt{\frac{\eta \rho_n \omega}{2}} dS, \quad (3)$$

where du_t/dr_n represents the derivative of the tangential velocity component in the direction normal to the surface element, which itself moves with a local velocity u_L . In the approximate expressions, α is a flow enhancement factor of order unity ($\alpha = 3/2$ for a sphere and $\alpha = 2$ for an infinite cylinder) that expresses the ratio of the velocity amplitude of the potential flow just outside the boundary layer to the velocity amplitude of the body. The average energy dissipated due to viscous friction by such a surface element over one period of oscillation is thus:

$$d\langle \dot{E}_f \rangle = \frac{\alpha u_{L0}^2}{2} \sqrt{\frac{\eta \rho_n \omega}{2}} dS, \quad (4)$$

with u_{L0} representing the local velocity amplitude. Integrating over the surface area of an oscillator, we arrive at:

$$\langle \dot{E}_f \rangle = \frac{\alpha \xi U_p^2 S_{\text{eff}}}{2} \sqrt{\frac{\eta \rho_n \omega}{2}}. \quad (5)$$

where U_p is the maximum velocity amplitude (peak velocity) along the surface of the resonator. The dimensionless quantity of order unity $\xi = \oint u_{L0}^2 dS / (S_{\text{eff}} U_p^2)$ describes the velocity profile along the resonator, and an effective surface area $S_{\text{eff}} \geq S$ may be used to account approximately for the surface roughness and other geometric effects. Conversely, a peak dissipative force may be defined as:

$$F_p = \frac{2\langle \dot{E}_f \rangle}{U_p} = \alpha \xi \omega S_{\text{eff}} U_p \sqrt{\frac{\eta \rho_n \omega}{2}}. \quad (6)$$

The total energy contained in the resonator is given as $E = m_{\text{eff}} U_p^2 / 2$, defining the effective mass of the resonator, m_{eff} . For a quasi one- or two-dimensional resonator oscillating perpendicularly to its large dimension(s) – such as a thin cantilever, beam, or membrane –

it follows that $m_{\text{eff}} = \xi m$, where m is the actual mass of the resonator. In such a case, it is convenient to define a fluidic quality factor, Q_f :

$$\frac{1}{Q_f} \equiv \frac{\langle \dot{E} \rangle}{\omega E} = \frac{\alpha S_{\text{eff}}}{m} \sqrt{\frac{\eta \rho_n}{2\omega}} = \frac{\alpha \rho_n S_{\text{eff}} \delta_n}{2m}, \quad (7)$$

which is independent of the oscillator velocity in the laminar regime. This expression differs from the one given in Ref. 1 by the explicit inclusion of the flow enhancement factor α . We note that this factor is related to the potential flow outside the boundary layer and is necessary to recover correctly the analytical solutions obtained for the drag force acting on an oscillating sphere or cylinder. In previous work, a significant effort has been made to study the dynamical response of rectangular beams immersed in viscous fluids systematically⁴⁶, but to our knowledge analytical expressions exist only for circular beams or beams with much greater width than thickness. This is not the case for the tines of the tuning fork used here and thus for the oscillators discussed further, we consider α a parameter to be determined experimentally.

Alternatively, the dissipative forces may be described in terms of a dimensionless drag coefficient. Following the definition of the drag coefficient in steady flow, the dimensionless drag coefficient related to the normal component becomes:

$$C_D^n = \frac{2F_p}{A\rho_n U_p^2} = \frac{2S_{\text{eff}}}{AU_p} \sqrt{\frac{\eta\omega}{\rho_n}}, \quad (8)$$

where A is the section area in the direction perpendicular to the flow. In accord with the principle of dynamical similarity, the drag coefficient may be expressed in terms of the Donnelly number:

$$C_D^n = \Phi / \text{Dn}, \quad (9)$$

where $\Phi = 2\alpha\xi S_{\text{eff}}/A$ is determined purely by the geometry of the oscillator. We see that in the laminar case, the drag due to the normal component is fully described by laws of classical fluid dynamics. Furthermore, by evaluating both the scaling function $f(\text{Wi})$ (where Wi is the Weissenberg number, see below) and the drag coefficient $C_D^n(\text{Dn})$ simultaneously, we are able to determine the geometric parameters. The factor αS_{eff} can be determined either from $f(\text{Wi})$ in the Newtonian limit, or with the velocity profile along the oscillator ξ and the section area A known, it can be obtained from the dependence of the drag coefficient on the Donnelly number.

In turbulent flow, we expect a constant value of the drag coefficient, as long as it is only the normal component that contributes to the drag force. On the other hand, if the superfluid component becomes turbulent at some critical velocity U_C , we expect a marked increase in the drag coefficient C_D^n above the dependence measured in a fully classical fluid. The Donnelly-Glaberson instability leading to the production of quantized vorticity in the superfluid is related to self-reconnection of seed vortex loops. This process has been sufficiently discussed in

the literature^{47,48}, and the related critical velocity is expected to scale as $U_C \propto \sqrt{\kappa\omega}$. Hence, it is convenient to define a reduced dimensionless velocity $\hat{U} = U/\sqrt{\kappa\omega}$. To facilitate the hydrodynamic description of the drag forces originating in superfluid component, we also define the superfluid drag coefficient:

$$C_D^s = \frac{2F}{A\rho_s U^2} = \frac{2F}{A\rho_s \kappa \omega \hat{U}^2}. \quad (10)$$

In the turbulent drag regime, at velocities sufficiently above the critical values, the normal and superfluid components of He II are expected to be coupled due to the mutual friction force and contribute to the pressure drag together. In this situation, the classical definition of the drag coefficient may be used: $C_D = 2F/(A\rho U^2)$, where the total density of He II $\rho = \rho_n + \rho_s$ is used. It is expected that in coupled turbulent flows, this drag coefficient will tend towards a temperature-independent constant value^{44,49} of order unity.

Note in passing that the described approach is approximate in the sense that it neglects the steady streaming flow that is known to exist in the vicinity of the oscillating objects and has been recently visualized in He II in highly turbulent flow due to vibrating quartz tuning fork³⁹. However, the streaming flow has negligible effect on the drag forces measured in laminar viscous flow as the typical length scale associated with streaming are of order of the size of the oscillator, while the boundary layer thickness is at least an order of magnitude lower in our experiments. In turbulent flows, the pressure drag is significantly larger than both the viscous friction and any additional drag due to the streaming. A brief discussion of other potential dissipation mechanisms follows at the end of this Section.

D. Ballistic Regime

In classical fluids, when the molecular mean free path λ becomes comparable to a characteristic dimension of the system D , or the angular frequency of the flow ω becomes comparable to the inverse of the relaxation time τ of the fluid towards equilibrium, the continuum hypothesis or the Newtonian description of the flow starts to break down and the system in question can no longer be described by the Navier-Stokes equations. On a fundamental level, such systems are characterized by a particle distribution function evolving according to the Boltzmann kinetic equation. In the transitional regime, where $\lambda \simeq D$ (or $\omega\tau \simeq 1$), extensions of the continuum approach are often employed, and quantities of interest are typically calculated as series expansions in terms of the Knudsen number $\text{Kn} = \lambda/D$, or the Weissenberg number $\text{Wi} = \omega\tau$. This typically happens in gases at low pressures of order 1 Pa, or in viscoelastic media.

In superfluid helium, a similar situation occurs in the normal component as the temperature is reduced below 1 K. Since the excitation density decreases very rapidly

with decreasing temperature, the mean free path of thermal excitations making up the normal component becomes comparable with the typical dimensions of the experiment around 0.7 K. Hence below 0.7 K, He II is better described as a gas of thermal quasiparticles propagating ballistically through a physical vacuum of the superfluid component^{50,51}, which only enhances the effective masses of accelerating objects, but exerts no drag force unless quantized vorticity is produced. Experimental observations of these effects have been made, e.g., with vibrating wires⁴¹, spheres²³, or grids²⁹.

Despite the notable differences in the underlying physics, a formalism may be developed relating the gas of thermal quasiparticles to classical dilute gases. This formalism may be used to directly compare measurements in superfluid helium to the results obtained in classical gases using MEMS/NEMS structures^{1,7,8}, which indicate a universal description of the drag forces in oscillatory flows. Verifying the proposed universality relation in a **gas of massless quasiparticle excitations** would yield very strong evidence in its support, especially considering that the range of experimentally attainable pressures may be extended by several orders of magnitude in superfluid helium. To make a direct comparison possible, we need to define the pressure, density, mean free path and relaxation time of the thermal excitations.

The dispersion relation of thermal excitations in ⁴He has been suggested by Landau¹⁶, and later verified in neutron diffraction experiments⁵². Long-wave excitations correspond to sound quanta and are called phonons, while excitations with higher momenta located around a minimum in the dispersion relation are traditionally called rotons. Statistical description of thermal excitations in ⁴He is usually carried out by considering phonons and rotons separately, ignoring excitations with higher energies due to their low occupation densities. Phonons are then approximately described by a linear dispersion relation $\epsilon_{\text{ph}} = cp$, where ϵ_{ph} is phonon energy, c is the (first) sound velocity, and p is momentum, while roton energies follow $\epsilon_{\text{rot}} = \Delta + (p - p_0)^2/(2m_r)$, where Δ is the roton gap, p_0 the roton momentum and m_r the roton effective mass.

Approximations of thermodynamic quantities related to phonons and rotons can be obtained from a statistical description of both types of excitations as (non-interacting) ideal Bose gases⁵³, with a possible simplification for the rotons, which may be treated as a classical Boltzmann gas at temperatures sufficiently below the roton gap $\Delta/k \approx 8.65$ K, where k is the Boltzmann constant. The grand partition function Z is given in the Thomas-Fermi approximation as:

$$\ln(Z) = - \int_0^\infty \frac{d^3\mathbf{p}}{(2\pi\hbar)^3} \ln(1 - e^{-\epsilon/kT}). \quad (11)$$

The free energy, pressure, entropy and heat capacity for both types of excitations can be obtained from the partition function using standard thermodynamic relations, while the number density of excitations is more

readily obtained by integrating the Bose-Einstein distribution $f_{\text{BE}}(\epsilon) = (\exp(\epsilon/(kT)) - 1)^{-1}$. Integration from zero to infinity instead of the corresponding ranges of momenta produces negligible errors as the high energy states are in first approximation statistically insignificant. To match macroscopic properties, the mass densities of phonons and rotons, ρ_{ph} , ρ_{rot} , are traditionally derived from considerations of momentum associated with the flow of the normal component in a frame of reference, where the superfluid is at rest⁵³. It is expected that $\rho_{\text{ph}} + \rho_{\text{rot}} = \rho_n$ at **temperatures below ≈ 1.5 K**, where all the assumptions of Landau's microscopic model hold with good accuracy.

The distributions of thermal excitations follow a kinetic equation of the Boltzmann type, with collision integrals determined by the relevant quantum scattering processes, but generally, processes corresponding to excitation emission and absorption must be taken into account as well⁵³. The excitation mean free paths and relaxation times are thus significantly more challenging to define precisely, as they depend on exact details of various types of multi-excitation processes occurring in He II. Analytical expressions for relaxation times may be derived approximately only for particular scattering processes⁵⁴, while a complete description remains impossible without intensive numerical calculations.

At temperatures below ≈ 0.6 K, the situation is greatly simplified, as the roton density becomes so low that rotons cease to affect the behavior of He II in a statistically significant manner and may be neglected (roton-roton and phonon-roton scattering become extremely rare events). Limiting ourselves to temperatures below 0.6 K and phonon excitations only, analytical treatment becomes possible⁵⁴ and has been tested, e.g., by experiments with vibrating wires⁴¹. For convenience, the energy per unit volume, pressure, mass density and number density of the phonon gas are given below, respectively:

$$\begin{aligned} E_{\text{ph}} &= \frac{\pi^2 (kT)^4}{30c^3\hbar^3} \\ P_{\text{ph}} &= \frac{\pi^2 (kT)^4}{90c^5\hbar^3} = \frac{1}{3} E_{\text{ph}} \\ \rho_{\text{ph}} &= \frac{2\pi^2 (kT)^4}{45c^5\hbar^3} = \frac{4}{3} \frac{E_{\text{ph}}}{c^2} \\ n_{\text{ph}} &= \frac{\zeta(3) (kT)^3}{\pi^2 c^3\hbar^3} \approx \frac{E_{\text{ph}}}{2.7kT}, \end{aligned}$$

where ζ is the Riemann zeta function, and $\zeta(3) \approx 2.4$. Since, fundamentally, the phonons behave like radiation quanta in that they have a zero rest mass, one might naively expect the energy per unit volume and mass density to be related by $E_{\text{ph}} = \rho_{\text{ph}} c^2$. However, the excitation mass density based upon equating the momentum of thermal excitations with the momentum of the macroscopic normal component^{16,53} does not obey Einstein's equation exactly, differing by a factor of 4/3, which can be explained from relativistic fluid dynamics. Indeed, if all particles in a gas propagate with a common (maximum) velocity c and satisfy the ultra-relativistic equation

of state $P = E/3$, where E is the energy per unit volume and P the pressure, ultra relativistic fluid dynamics may be used to describe the system. Then the fluid momentum density is given by $\mathbf{p} = \mathbf{v} (E+P)/c^2$, see pp. 505-506 in Ref. 55. The sum $E + P$ corresponds to enthalpy per unit volume $H = 4E/3$, which determines the energy flux density in a classical ideal fluid $\mathbf{j}_E = H\mathbf{v}$. Since, in the phonon gas, momentum and energy are directly related by the dispersion relation $E = cp$, the enthalpy appears in the expression for the momentum density as well, and leads to the above mentioned factor of $4/3$. It is also important to note that the speed of propagation of sound waves in the ultra-relativistic phonon gas, which corresponds to second sound in He II in the zero temperature limit, is given by $c_2 = c/\sqrt{3}$.

The most important types of scattering events in the phonon gas at $T < 0.6$ K are three-phonon processes (3pp) occurring at small scattering angles and four-phonon processes (4pp), which are important for large scattering angles. For a detailed discussion, we refer the reader to the work of Adamenko *et al.*⁵⁶ and other notable works on the topic^{57,58}. Here, we will use the results of Ref. 56 obtained by solving the kinetic equations in the relaxation time (BGK) approximation that are in agreement with the experiments of Greywall⁵¹ and of the Kharkov laboratory⁵⁹. Below 0.6 K one may thus establish a temperature-dependent phonon relaxation time τ_{ph} and mean free path λ_{ph} . At temperatures between 0.2 K and 1.0 K, the mean free path of Ref. 56 may be approximated with sufficient precision as:

$$\log_{10}(\lambda_{ph,eff}[m]) = a_0 + a_1T + a_2T^2 + a_3T^3 + a_4T^4, \quad (12)$$

with T in kelvin and the coefficients given as $(a_0, a_1, a_2, a_3, a_4) = (3.829, -26.37, 35.86, -25.17, 6.862)$.

This corresponds to curve (1) in Fig. 2 of Ref. 56, which describes an effective mean free path based on a computed relaxation time, i.e., we may use $\lambda_{ph,eff} = c_2\tau_{ph}$. In the language of Ref. 57 this corresponds to a “viscosity mean free path”, and indeed ought to be comparable with mean free path determined from experimental measurements of viscosity using $\eta = \rho_{ph}\tau_{ph}c_2 = 1/3\rho_{ph}c\lambda_{ph,exp}$.

We should thus bear in mind that the actual phonon mean free path λ_{ph} is limited by 3pp occurring at small angles and is significantly smaller than $\lambda_{ph,eff}$. Based on the estimates of Benin and Maris⁵⁰, the actual mean free path would be $\lambda_{ph} \approx 10^{-4}\lambda_{ph,eff}$ with a typical scattering angle γ , between 5 and 10 degrees, where the factor relating the two mean free paths⁵⁷ is proportional to γ^4 . It is, however, $\lambda_{ph,eff}$ that is relevant for a fluid-dynamical description.

Temperature-dependent phonon Knudsen and Weissenberg numbers may be defined as $Kn_{ph} = \lambda_{ph,eff}/L$, $Wi_{ph} = \omega\tau_{ph}$. These dimensionless parameters are plotted in Fig. 1 against temperature for $L = 75 \mu m$ for particular frequencies $f = \omega/(2\pi) = 6.4$ kHz and 40.0 kHz, which corresponds to the 6.4 kHz tuning fork discussed further oscillating in its fundamental mode and first overtone, respectively. According to Ekinici *et al.*¹, a bound-

ary layer Knudsen number Kn_δ would scale proportionally to Wi_{ph} and is not included. Fig. 1 shows the importance of the ballistic treatment below ≈ 0.7 K and of non-equilibrium (non-Newtonian) description at lower temperatures, depending on the frequency of the mode in question. Note that we consider the Knudsen and Weissenberg numbers well-defined only for $T < 0.6$ K, as discussed above.

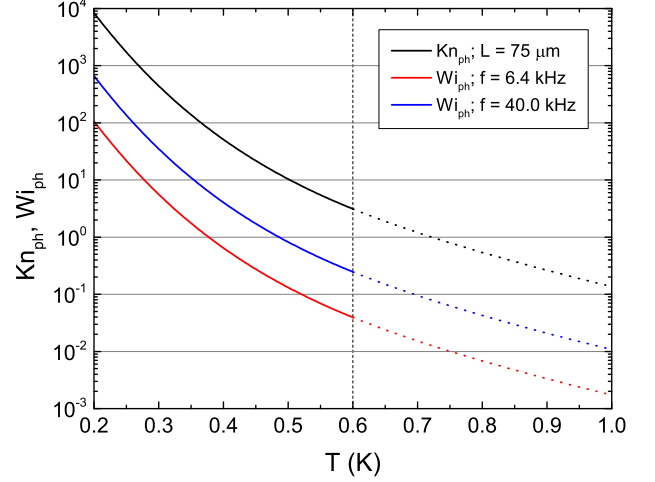


FIG. 1. Phonon Knudsen number (for $L = 75 \mu m$) and Weissenberg numbers (for $f = 6.4$ kHz and 40.0 kHz) plotted against temperature. The dashed line separates the interval of temperatures $T < 0.6$ K, where the properties of He II are reliably described by phonon scattering processes only (solid lines), from the range, where the dynamics of He II might become influenced by the presence of rotons, leading to increasing rates of phonon-roton scattering and deviations from the dependences shown (dotted lines).

E. Universal Scaling Relation

In Ref. 1, an extended solution to Stokes’ second problem (an oscillating plane) is presented, based on a relaxation time (BGK) approximation of the Boltzmann kinetic equation. The velocity field is given in Eq. (17) in the reference and two length scales related to the boundary layer are defined, a penetration depth, δ_- , and a wavelength δ_+ , which differ from the original viscous penetration depth by a factor expressed as a function of $Wi = \omega\tau$. This solution is used to derive a universality relation valid in the high frequency limit at low velocities (at which no turbulence is produced) across both Newtonian and non-Newtonian regimes of the fluid. Using a scaling function $f(\omega\tau)$, the authors relate the fluidic quality factor of the resonator with geometric and hydrodynamic parameters, see Eqs. (23) and (24) in Ref.¹. We adapt the relation for the normal component of He II

and include the flow enhancement factor α , leading to:

$$\frac{1}{Q_f} = \frac{\alpha S_{\text{eff}}}{m} f(\text{Wi}) \sqrt{\frac{\eta \rho_n}{2\omega}} \quad (13)$$

$$f(\text{Wi}) = \frac{(1 + \text{Wi}) \cos(\phi) - (1 - \text{Wi}) \sin(\phi)}{(1 + \text{Wi}^2)^{3/4}} \quad (14)$$

$$\phi = \frac{\tan^{-1}(\text{Wi})}{2} \quad (15)$$

In the ballistic regime, the relaxation time, Wi , and other parameters entering the previous equation are given above. The flow enhancement factor is well-defined in the hydrodynamic regime only, but we may keep it for simplicity, putting $\alpha_b = 1$ in the ballistic regime below 0.6 K. In the hydrodynamic regime, the relaxation time of the normal component may be defined from the viscosity using a relation *analogical* to that employed in standard kinetic theory: $\eta = \rho_n \tau c_2^2$, leading to $\text{Wi} = \eta \omega / (\rho_n c_2^2)$. This allows us to use the scaling relation both for the hydrodynamic regime above 1 K and for the phonon gas below 0.6 K. Substituting for the viscosity in Eq. 13, this equation may be re-written as:

$$\frac{1}{Q_f} = \frac{\alpha \rho_x S_{\text{eff}} c_2}{m \omega} \sqrt{\text{Wi}/2} f(\text{Wi}), \quad (16)$$

with ρ_x meaning either ρ_n or ρ_{ph} in the hydrodynamic and ballistic regimes, respectively. In Section VB, we will use this form of the proposed universality relation for comparison against experimental data. The transitional regime at intermediate temperatures between 0.6 K and 1.2 K is also discussed in Ref. 60.

F. Multiple Critical Velocities in the Superfluid

Here we comment briefly on the transition to turbulent drag regime observed in the superfluid at very low temperatures corresponding to the ballistic regime. In oscillatory flows under these conditions, a number of experimental studies *utilizing* wires⁴², grids^{27,28} or tuning forks^{32,61} reported observation of more than one critical velocity of hydrodynamic origin. Recently we have presented convincing evidence for three distinct hydrodynamic critical velocities and proposed explanation linking all the observations of oscillatory flow in zero temperature limit into a single framework³⁴.

The first critical velocity, connected mostly to frequency shifts rather than changes in the drag force, is associated with the formation of a number of quantized vortex loops near the surface of the oscillator, possibly forming a thin layer, which affects the coupling to the fluid and thus the hydrodynamic added mass. This first critical velocity is hardly observable in the two-fluid regime above 1 K. The second critical velocity is related to the quantized vorticity propagating into the bulk of the superfluid, either in the form of emitted vortex loops

or, eventually, as a turbulent tangle. It is always accompanied by a marked increase in the drag force and usually hysteresis (detectable with amplitude sweeps). We would like to stress that it is this critical velocity which we will be discussing later in relation to the experiments performed in the hydrodynamic regime above 1 K.

For completeness, there is the third and highest critical velocity of hydrodynamic origin, above which the drag coefficient starts to grow towards unity even at mK temperatures, where constant values of order 10^{-1} or 10^{-2} are typically reported at velocities exceeding the second, but not the third critical velocity. As the observed *third* critical velocity was very high, always above 1 *ms*⁻¹, it is very unlikely that it was reached in the experiments reported here.

G. Additional Dissipation Mechanisms

In our recent work³⁴ we investigated the behavior of oscillatory flow due to quartz tuning fork in isotopically pure superfluid He II in the zero temperature limit. We have shown that the linear damping forces can be fully described and understood as a combination of tuning fork intrinsic damping (dominant at lowest temperatures) and ballistic phonon drag $\propto T^4$, which gradually changes into hydrodynamic viscous damping at higher temperatures. In addition to viscous damping, losses due to sound emission through the surrounding fluid may occur, and may be accounted for approximately⁶². In the present work, acoustic losses can be safely neglected for the fundamental mode of the tuning fork and represent perhaps a very small contribution to the damping of its first overtone⁶³. Based on our previous studies of acoustic emission by oscillating objects in He II^{62,63}, acoustic losses are negligible for all other oscillators used in this work. In our experiments, no sign of cavitation and associated losses was detected.

III. EXPERIMENTAL DETAILS

Most of the resonators used in our investigation – the wire, the tuning fork, and the double paddle – were driven by an Agilent A33220 signal generator, and a phase-sensitive Stanford Research SR830 lock-in amplifier was used to measure both the in-phase and out-of-phase components of the induced signals.

Most of the measurements were performed in a helium immersion cryostat during a dedicated experimental run for each resonator. The helium bath is brought down to the desired temperature using a rotary pump and a Roots pump and stabilized on the level of few mK either by manually adjusting the pumping speed, or using a temperature controller. The lowest attainable temperature of 1.27 K allows access to most of the hydrodynamic (two-fluid) regime.

Measurements at sub-K temperatures in the ballistic regime were performed on a Leiden Cryogenics MNK126-400 dilution refrigerator with a base temperature below 10 mK. The cell containing the oscillators was flushed repeatedly with dry nitrogen gas prior to cooling to 10 mK under vacuum. It was then filled very slowly, over a period of 48 hours, with isotopically pure superfluid ^4He .

A. Vibrating Wire Resonator

Vibrating wire resonators are well-established low temperature probes⁶⁴. They consist of a semi-circular loop of wire subjected to a vertical magnetic field B , as shown in Fig. 2. A loop is used to prevent closely spaced or degenerate resonant modes one may observe on a straight wire.

Passing an alternating current $I(\omega)$ through the wire forces it to oscillate due to the Lorentz force, $F_L = BDI$. As the wire moves through the magnetic field, it induces a voltage which can be determined using Faraday's law. For a rigid semi-circular wire with leg spacing D , oscillating at a peak velocity U , the area bounded by the loop $A = \pi D^2/8$ and the rate of change of angle to the field is $2U/D$. Therefore, the induced Faraday voltage generated by a semi-circular vibrating wire loop is given by:

$$V = -\frac{d(\mathbf{B} \cdot \mathbf{A})}{dt} \simeq \frac{\pi}{4} BDU. \quad (17)$$

The vibrating wire resonator used in this study consists of a semi-circular loop $40\ \mu\text{m}$ superconducting NbTi wire with a leg spacing of 2 mm. The wire was mounted in a brass cell submerged in the bulk superfluid and mounted between a pair of permanent magnets in a magnetic field of $170 \pm 10\ \text{mT}$ at room temperature. We estimate that the field is reduced by approximately 20% at low temperatures⁶⁵.

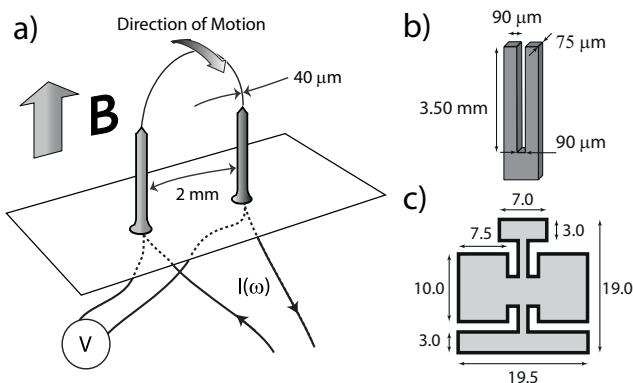


FIG. 2. Schematic diagrams of the vibrating wire resonator (a), of the quartz tuning fork (b), and the double paddle (c). The dimensions of the double paddle are in millimeters. The wafer thickness is $75\ \mu\text{m}$ for the tuning fork and $250\ \mu\text{m}$ for the double paddle.

B. Quartz Tuning Fork

Quartz tuning forks are piezoelectric oscillators with a calibrated resonant frequency, often used as frequency standards or shear force sensors for scanning optical microscopes⁶⁶. Quartz tuning forks are now well-established probes of cryogenic helium flow³¹. The fork used in this study is of the following dimensions: length of the prongs $L_f = 3.50\ \text{mm}$, tine thickness (parallel to the direction of motion) $T_f = 90\ \mu\text{m}$ and width $W_f = 75\ \mu\text{m}$ (original wafer thickness). Its two prongs are separated by $D_f = 90\ \mu\text{m}$. A sketch of the fork including these dimensions is shown in Fig. 2. There are two different readily accessible flexural resonant modes – the fundamental resonance at 6.5 kHz and the first flexural overtone at 40.0 kHz.

The fork is driven by applying an ac voltage V from a function generator to the metallic electrodes deposited on the surface of the quartz. This produces a force proportional to the voltage which sets the two prongs oscillating in anti-phase along the direction T_f . The distortion of the quartz induces a piezoelectric-current I which is proportional to velocity U . The relations between force, velocity, voltage and current are:

$$F = \frac{a_f V}{2} \quad I = a_f U; \quad (18)$$

where a_f is the so-called fork constant, which may be obtained through calibration by deflection measurement or self-calibration in vacuum, in which case it is given as $a_f = \sqrt{4\pi m_f^{\text{eff}} \Delta f I / V}$, where m_f^{eff} is the effective mass of the fork, and Δf is the measured half-height resonant width³¹. The effective mass⁶³ of the tuning fork is given by $m_f^{\text{eff}} = T_f W_f L_f \rho_q / 4$, where $\rho_q = 2650\ \text{kgm}^{-3}$ is the density of the fork material (quartz). The ac current is measured using an IV-converter⁶⁷ and a SR-830 lock-in amplifier. The standard measurement scheme used here can be found, e.g., in Fig. 1 of Ref. 34.

C. Double Paddle

Recent studies^{37,38} have shown that the so called double-paddle resonators may serve as promising probes to study superfluid hydrodynamics. These have demonstrated high quality factors, compared to other mechanical resonators since any vibrational losses through their base are heavily suppressed.

Here, we employ the same silicon double paddle oscillator etched from a 0.25 mm thick $\langle 110 \rangle$ silicon wafer, as previously used by Zemina and Luzuriaga³⁷, sketched in Fig. 2. The two larger side paddles are approximately $10\ \text{mm} \times 7.5\ \text{mm}$ and the smaller upper paddle is $7\ \text{mm} \times 3\ \text{mm}$. The paddle is driven magnetically, by attaching a small magnet located between the paddles in the oscillator stem; its displacement is detected capacitively. In order to generate the oscillatory motion, an ac current

is applied to a small superconducting coil fixed to the support frame.

D. Torsionally Oscillating Disc

The torsional oscillator consists of a 0.05 mm tungsten wire 32 cm long with a borosilicate glass disc fixed to the wire at its midpoint using a thin 0.8 mm brass capillary and Stycast 2850 GT. The disc is 1 mm thick with a diameter of 40 mm; a schematic diagram is shown in Fig. 3. When the wire is under tension, the disc is positioned approximately midway between the two polished FR2 plates 10 mm apart (both disc sides were approximately 4.5 mm away from the FR2 plate facing them). Sixteen black marks around the circumference of the disc are used to determine the deflection and angular velocity of the disc from recorded video sequences.

The motion of the disc is recorded with a Canon EOS 600D digital camera fitted with a Canon EF-S 18-135 mm f / 1:3.5 - 5.6 IS lens. The recordings were acquired at the frame rate of 240 fps with a resolution of 512×384 pixels. A large optical lens was used to improve the scale resolution.

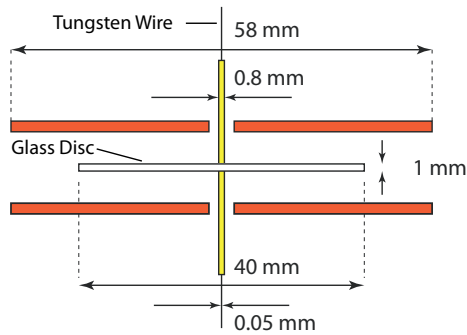


FIG. 3. Schematic diagram of the torsionally oscillating disc.

Our raw data is in the form of video recordings of the motion of the disc during the experiments. Because the marks on the disc are relatively small compared to the entire field of view, with rather low contrast to the not-entirely-uniform background, standard motion tracking software could not be used to process the videos. Hence, fairly complex post-processing is required to extract quantitative and interpretable data.

The videos are split into individual frames and de-interlaced in the process, which means that only pixels recorded at exactly the same time are kept for each frame. The color images are converted to monochromatic bitmaps by dynamic contrast algorithms implemented in NI VISION software, so that the marks appear as black spots on a white background. These monochromatic bitmaps are then analyzed by a custom-made LabVIEW program. In the first pass, the program localizes the black areas in each image and evaluates their size and center-of-mass. In the second pass, using only numer-

ical data from the first pass, it then links corresponding images of the same dot between all frames to each other (making special arrangements for those not reproduced in some of the bitmaps) and calculates the angular displacement of the disc in each instant using a self-calibration obtained by a complete revolution of the disc around its axis. The optical distortion from the lenses and the curved walls of the glass cryostat are negligible, as only a 10 mm central portion of the field of view is used in the processing.

IV. EXPERIMENTAL RESULTS AND ANALYSIS

In this Section we present our drag force measurements by using the resonators introduced above, starting with the hydrodynamic regime. We isolate the sources of the various drag forces acting on the structures, in particular, by separating the contributions due to the two fluid components.

In our previous study of tuning forks in He II at very low temperatures³⁴, it was shown how important it is to perform full frequency sweeps across the resonant response of the oscillators. These full sweeps, at fixed drive level, reveal important details relevant to the onset and the nature of any nonlinear behavior, displaying complex features in the resonant response such as various nonlinear phenomena. On the other hand, simple and less time consuming amplitude sweeps at fixed resonant frequency might uncover hysteretic features that might otherwise have been overlooked by amplitude sweeps, and we therefore paid attention to check the resonant response in both ways.

A. Vibrating Wire Resonator

The resonant response of the vibrating wire resonator is obtained by measuring the voltage in phase with the driving current, as a function of frequency. In Fig. 4, we plot the resonant frequency response of the vibrating wire at various drives at 1.67 K. The velocity of the top part of the wire is known with the accuracy about $\pm 20\%$, as the actual value of the magnetic field produced by the pair of permanent magnets has not been calibrated at low temperature. This does not affect the scaling of the drag discussed later, as long as the magnetic field remains constant. For small drive levels, the frequency response is of Lorentzian form. Upon increasing the drive level, the Lorentzian shape becomes distorted and the resonant frequency decreases. The flattening of the peak indicates the onset of non-linear drag forces typically associated with instabilities in the generated oscillatory flow.

In Fig. 5, we plot the peak velocity U as a function of driving force F at various temperatures. Each point represents the results of a pair of full frequency sweeps; one measured with increasing, the other with decreasing fre-

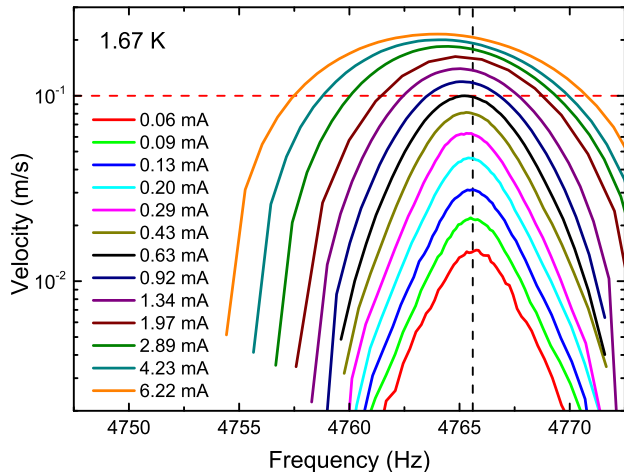


FIG. 4. Resonant frequency response of the vibrating wire resonator at various drives at a temperature of 1.67 K. The black vertical dashed line marks the position of the resonance peak at low drives. The red dashed line highlights the estimated velocity at which the frequency-softening sets in and the frequency shift becomes apparent.

quency, which allows us to identify any hysteretic behavior. At low velocities, the wire exhibits linear damping at

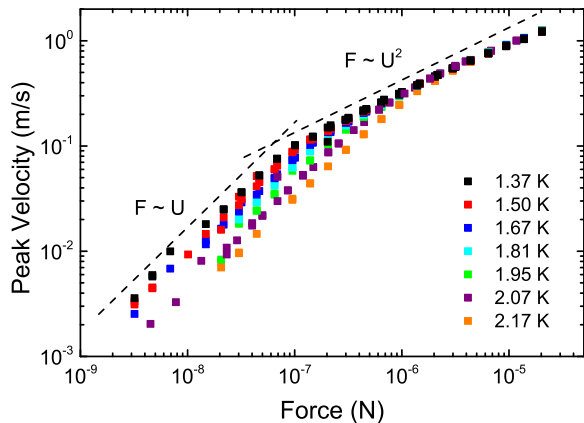


FIG. 5. Peak velocity as a function of the peak driving force applied to the vibrating wire submerged in superfluid ^4He at temperatures as indicated. The dashed lines serve as guides to the eye.

all temperatures. The **loses** from the wire in this region are dominated by temperature-dependent hydrodynamic viscous drag due to the normal fluid component, but in principle include intrinsic mechanical losses and acoustic emission as well - these **loses** are (for all oscillators used in this work) small, and are mentioned here just for completeness.

Upon reaching some critical velocity, the response changes, indicating an extra dissipation mechanism which eventually begins to dominate. The damping force

gradually becomes proportional to U^2 and independent of temperature T , in the studied temperature range, $1.293 \text{ K} \leq T \leq 2.170 \text{ K}$.

The classical drag coefficient as a function of velocity for the vibrating wire are plotted in Fig. 6; the drag coefficient being evaluated using the data presented in Fig. 5. To calculate the drag coefficient $C_D = 2F/(A\rho U^2)$ from the dissipative force F (which is equal to the driving force), we use the peak wire velocity U and A is the projected cross-section of the wire perpendicular to the wire's direction of motion: $A = d_w l_w$, where d_w is the wire diameter and l_w is the length of the loop.

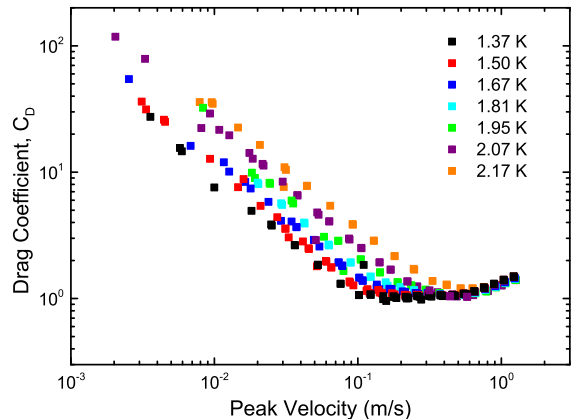


FIG. 6. Drag coefficient as a function of peak velocity for the vibrating wire at various temperatures as indicated.

In order to collapse the contribution of the normal fluid component to the drag forces acting on the wire to a single dependence, we plot the drag coefficient for the normal component as a function of the Donnelly number (see Eq. 9) in Fig. 7.

Universal scaling is observed for the wire, however, we note that the pre-factor for the laminar scaling is somewhat larger than one would expect for a smooth cylinder. This is most likely due to the surface roughness and excrescences left on the wire during the ablation of the wire's insulation and variations in the cross section of the wire caused by extrusion during the manufacturing process, effectively increasing the surface area of the wire and possibly introducing sharp corners leading to additional flow enhancement. **Under an optical microscope, individual irregularities of size greater than $5 \mu\text{m}$ were observed.**

B. Tuning Fork

The resonant response of the quartz tuning fork is again obtained by measuring the current in-phase with the driving voltage as a function of frequency. The electrical quantities are then converted into mechanical quantities, as explained in the previous Section. By per-

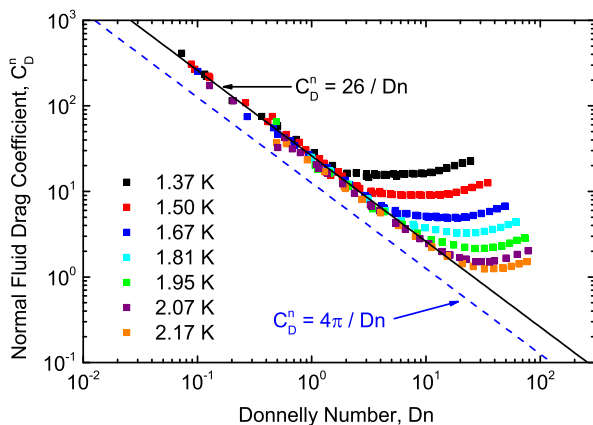


FIG. 7. Normal fluid drag coefficient as a function of the Donnelly number for the vibrating wire at various temperatures as indicated. The blue dashed line shows the expected dependence for a smooth cylinder at low velocities⁵⁵. The solid black line is an empirical fit to the linear data. The temperature-dependent departure points from the viscous damping are a clear sign of the onset of damping due to the superfluid component. The data obtained at 2.17 K are an approximate indication of the behaviour of the wire in any classical fluid.

forming frequency sweeps in vacuum at low temperature, the experimental fork constant is estimated to be $a_f = 3.665 \times 10^{-7} \text{ C/m}$ and $a_f^o = 1.409 \times 10^{-6} \text{ C/m}$ for the fundamental mode and first overtone, respectively.

On resonance, the driving force is in equilibrium with the dissipative drag force acting on the prongs. The power dissipated by the two prongs of the tuning fork is assumed to be equal to the supplied electrical power given by $\dot{Q} = IV/2 = F_p U_p$, where F_p is the peak force acting on one prong and U_p is its peak velocity. We estimate that the fork constant has an uncertainty of 10% since it was shown that the optically-measured prong velocity is actually 10% lower⁶⁸ than that determined from the electro-mechanical model described in Section III B.

In Fig. 8, we plot the classical drag coefficient as a function of the peak velocity for the fundamental mode of the fork at various temperatures. To calculate the drag coefficient from the peak dissipative force F_p , we have assumed that A equals to the cross-sectional area of a tuning fork prong perpendicular to its motion, $W_f L_f$, and we use the tuning fork peak velocity U_p . As expected, the tuning fork exhibits linear damping at low velocities at all temperatures. Upon increasing the velocity, changes in the drag coefficient's velocity dependence can be observed occurring at approximately 10^{-1} m/s and are independent of temperature in the assessed temperature range.

At high velocities, the drag coefficient tends to a temperature-independent constant value of order unity ($C_D \approx 0.6$) as one would expect for a classical fluid. One might anticipate that, at very high velocities, the drag will no longer depend on whether the fluid is superfluid or

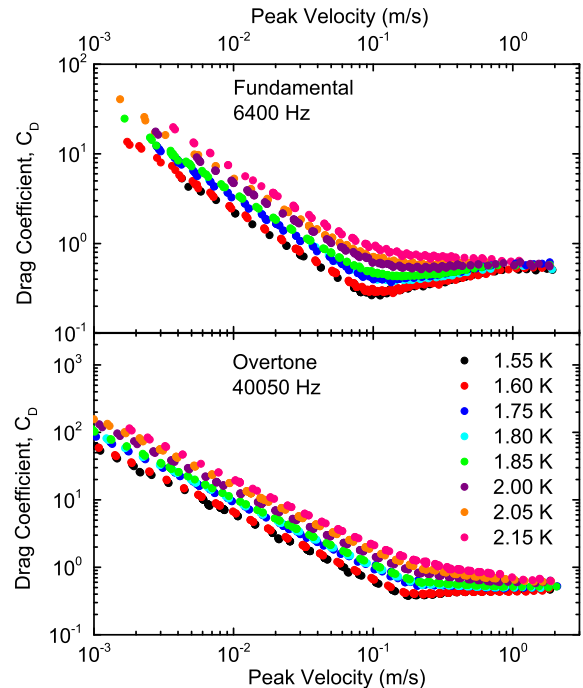


FIG. 8. Dimensionless drag coefficient as a function of peak velocity for the fundamental mode (Top) and overtone (Bottom) of the tuning fork at various temperatures.

not, as the pressure drag is expected to dominate in fully turbulent flow. In our case, there is little variation in the drag coefficient at high velocities over the full temperature range and we therefore conclude that the two fluids must be coupled in the fork's vicinity by mutual friction and the flow due to the fork behaves as a single classical-like fluid in the turbulent drag regime. On decreasing temperature, the drag coefficient drops appreciably over the range of low and intermediate velocities as the density of the normal fluid component decreases.

To characterize the flow of the normal component, we again plot the normal fluid drag coefficient as a function of the Donnelly number for both of the tuning fork's modes in Fig. 9. At low Donnelly numbers, the data from both modes collapse to a single dependence before deviating at some temperature-independent critical value. This critical Donnelly number marks the location of the instability in the flow of the normal component. The onset of the turbulent drag regime is thus governed by the value of the Donnelly number alone, **in contrast to the results obtained with the vibrating wire.**

It is interesting to note that despite the difference in the velocity profile and the viscous penetration depth, the same pre-factor Φ in Eq. 9 is obtained for the two modes of oscillation. This is due to the fact that both modes have, apart from the surface area, also the same flow enhancement factor α determined by the rectangular cross-section of the prong and the same effective mass $m_{\text{eff}} = \xi m$ with $\xi = 1/4$, see Appendix A of Ref. 63.

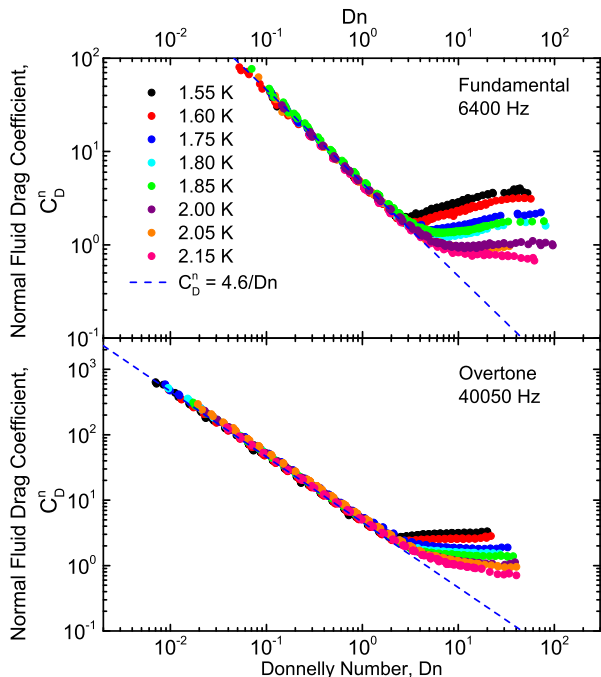


FIG. 9. Normal fluid drag coefficient as a function of the Donnelly number for the fundamental mode (Top) and the overtone (Bottom) of the tuning fork at the various indicated temperatures. The laminar drag (dashed lines) follows the same dependence for both modes given by $C_D^n = 4.6/Dn$.

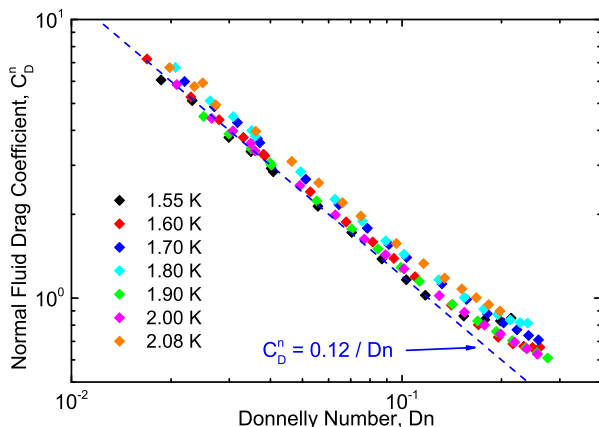


FIG. 10. Normal fluid drag coefficient as a function of the Donnelly number calculated for the silicon double-paddle of Zemma and Luzuriaga³⁷.

C. Double Paddle

We now apply the same analysis to results obtained using a silicon double paddle oscillator by Zemma and Luzuriaga³⁷. Specifically, we analyze the symmetric torsion mode data³⁶. In vacuum at 4.2 K, the resonant frequency of the paddle is 520 Hz, in liquid helium at 4.2 K it was 358 Hz. The viscous penetration depth

is $\approx 3 \mu\text{m}$. Since the characteristic length scale of the paddle is $D \approx 1 \text{ cm}$, the paddle is operating in the high Stokes number limit, which means that our analysis is justifiable.

In Fig. 10, we present the normal fluid drag coefficient plotted against the Donnelly number. The viscous drag force again collapses to a single dependence demonstrating that the paddle is indeed in the high Stokes number limit, and backing up our claim that scaling due to the drag force offered by the normal fluid is universal, following approximately $C_D^n = 0.12/Dn$.

Closer inspection of the data shows, however, that the source of the initial instabilities is not entirely clear. To address this, we plot the normalized non-linear drag force as a function of the Donnelly number for the double paddle in Fig. 11. At high temperatures (for $T \gtrsim 1.7 \text{ K}$), the instabilities appear to be governed by the Donnelly number and collapse, hence they must originate in the normal fluid component. On the contrary, at low temperatures, the governing parameter is the paddle's velocity, therefore the instabilities are of the Donnelly-Glaberson type and originate in the superfluid component.

It seems therefore that there is, within the covered temperature range, a cross-over of first instability which originates from the superfluid component at low temperatures and from the normal component at higher temperatures. We shall argue below that this behavior is easily observed also in the drag data from the flow due to the torsionally oscillating disc.

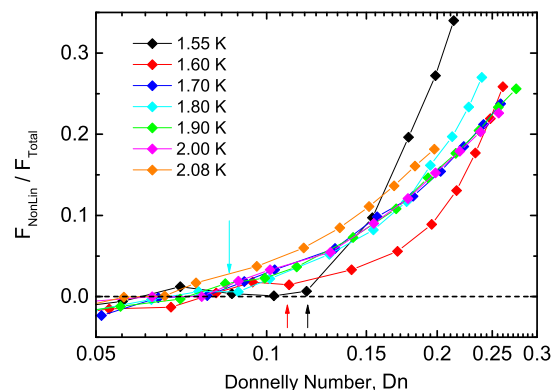


FIG. 11. Normalized non-linear damping force as a function of the Donnelly number of the silicon double-paddle. At higher temperatures, the non-linear damping is temperature independent and any deviation from this universal dependence is due to the contribution of the superfluid component. The black, red and cyan arrows indicate the Donnelly number where non-linear damping sets in at 1.55, 1.60 and 1.80 K, respectively. At 1.55 K and 1.60 K, the onset of nonlinear damping happens at a velocity very close to 1.0 mm s^{-1} , but for the higher temperatures, no well-defined critical velocity exists as the values are spread evenly between $\approx 0.2 \text{ mm s}^{-1}$ and $\approx 0.5 \text{ mm s}^{-1}$, with the lowest “critical velocity” corresponding to the temperature 2.08 K.

D. Torsionally Oscillating Disc

The torsionally oscillating disc differs from the previous oscillators in three fundamental ways. First, as the disc oscillates around its axis, it does not displace any fluid, hence there is no potential flow outside the boundary layer. Second, in this case we are not able to perform measurements in a steady state and we have to deal with a (slowly) decaying oscillation of the disc as well as decaying flow. Third, we cannot directly measure the drag force and have to infer the damping from the decaying amplitude of oscillation. Despite this important difference, we seek to analyse the flow in a manner similar to the above oscillators.

First, we have established that the intrinsic damping of the disc is negligible compared to that due to the surrounding helium. This was done by measurements in vacuum at room temperature and 78 K, and already at 78 K the vacuum damping was far below any measured in superfluid helium in the attainable range of temperatures.

To compare with other oscillators, we define a drag coefficient for a thin disc torsionally oscillating in a viscous fluid of density ρ_n as:

$$C_D^n = \frac{2M_F}{A\rho_n\Omega_0^2R^3}, \quad (19)$$

where M_F is the moment of friction forces, R is the disc's radius, $A = \pi R^2$ is the surface area of one side of the disc, Ω_0 is the amplitude of the angular velocity and ω is the angular frequency of oscillation. For a rationale of this definition, and for the derivation of the Donnelly number dependence, we refer the reader to Appendix VI, where we also show that in laminar flow, the drag coefficient due to the normal component can be expressed in terms

of the Donnelly number as $C_D^n = 2/Dn$.

As M_F cannot be obtained directly from the experiment, we have to infer the drag coefficient from other measurable quantities, such as the extremal displacements of the disc during its damped oscillations, such as shown in Fig. 12. If the series of extremal angular displacements occurring at times t_n is labeled Φ_n (interleaving maxima and minima in chronological order), the logarithmic decrements of the amplitude of oscillation α_n are determined as $\alpha_n = \ln(\phi_{n-1}) - \ln(\phi_{n+1})$ and the immediate angular frequency of oscillation is $\omega_n = 2\pi/(t_{n+1} - t_{n-1})$. This leads to an alternative definition of the drag coefficient:

$$C_D^n = \frac{2I\alpha}{\pi A \rho R^3 \phi_0} \simeq \frac{\rho_d h_d \alpha}{\pi \rho R \phi_0}, \quad (20)$$

where ϕ_0 the immediate angular displacement amplitude, and $I = I_0 + I_{HD}$ stands for the effective moment of inertia consisting of the moment of inertia of the disc itself, I_0 , and of its hydrodynamic enhancement, I_{HD} . If $I_{HD} \ll I_0$, the simplified expression on the right hand side of Eq. 20 holds, where ρ_d is the density of the disc

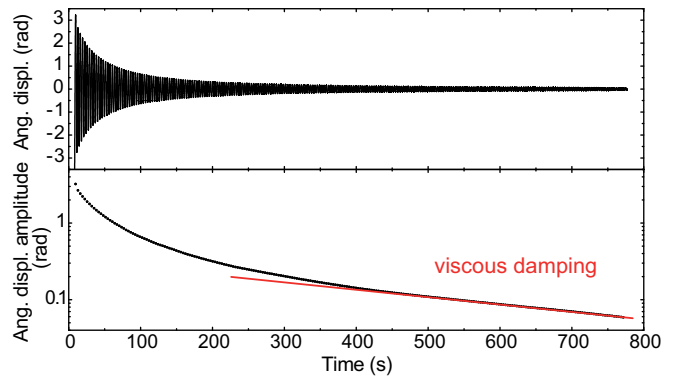


FIG. 12. Typical measurement of angular displacement of the torsionally oscillating disc as a function of time. (Top) The signal extrema were evaluated to obtain the angular displacement amplitude, ϕ_0 . The logarithmic plot (Bottom) clearly shows two distinct regions – exponential (viscous) decay due to laminar flow of the normal component for $t \gtrsim 500$ s and a faster nonlinear decay at earlier times.

material, and h_d the height (thickness) of the disc. The derivation can be again found in Appendix VI.

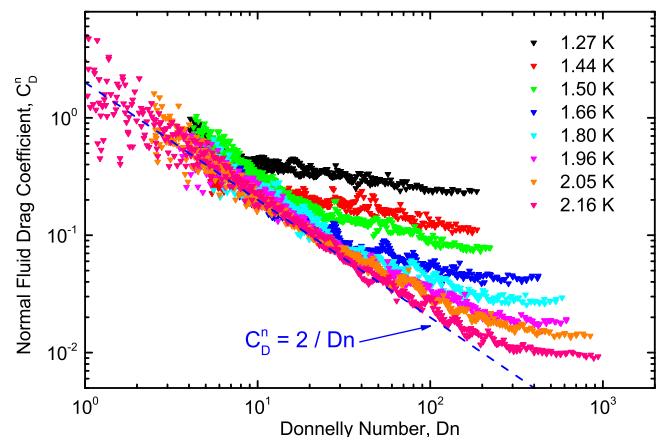


FIG. 13. Normal fluid drag coefficient as a function of the Donnelly number for the torsional disc at the various indicated temperatures. The dashed blue line is the predicted dependence for viscous drag $C_D^n = 2/Dn$.

We plot the drag coefficient C_D^n measured at various temperatures against the Donnelly number $Dn = \rho_n \delta_n R \omega \phi_0 / \eta$ in Fig. 13. Again, at small values of Dn , the data collapse to a single dependence illustrating the universal behaviour. One would naturally expect the drag coefficient to follow a $\propto 1/\phi_0$ dependence, the more that the superfluid component remains stationary in the laboratory frame of reference, similarly as in the famous experiment of Andronikashvili²². On the other hand, the instabilities clearly displayed in Fig. 13 are not characterized by any single value of Dn . This implies that the instability cannot be generally explained by viscous fluid dynamics of the normal fluid and must be related to the

superfluid component.

Since we are interested in the origin of the non-linear drag forces acting on the disc, the viscous damping was withdrawn from the the logarithms of the signal maxima in Fig. 12 and the signals were reprocessed. We will now discuss the flow of He II due to the torsionally oscillating disc in terms of dimensionless velocity defined as $\hat{U} = R\omega\phi_0/\sqrt{\kappa\omega}$, taking into account the work of Hänninen and Schoepe⁴⁸, who showed that the superfluid critical velocity scales proportionally to $\sqrt{\kappa\omega}$. Using the same logic as we used above to define C_D^s , we now define the superfluid drag coefficient as:

$$C_D^s = 2I\alpha\pi A\rho_s R^3\phi_0 \simeq \rho h_d\alpha/\pi\rho_s R\phi_0. \quad (21)$$

The drag coefficient C_D^s must remain close to zero until some critical **velocity** \hat{U}_c is reached, at which quantized vorticity becomes formed and some of the quantized vortices will reconnect to generate vortex loops which will propagate into the bulk superfluid, carrying with them some of the kinetic energy supplied by the oscillating disc. This process is experimentally observed as an increase in the drag coefficient C_D^s , which is plotted (after eliminating laminar drag contribution) as a function of the dimensionless velocity \hat{U} in Fig. 14. In the top panel, which shows no collapse of the data, we plot all our data, obtained at various temperatures. The situation is very different if only the data taken at 1.955 K and below are displayed, see the bottom panel of Fig. 14, where one observes a distinct critical value of the dimensionless velocity $\hat{U}_c \approx 12$. At these temperatures, the initial instability is most likely related to the production of quantized vorticity by a Donnelly-Glaberson type instability (vortex loop self-reconnection), since the non-linear contribution is temperature-independent, showing that the superfluid component undergoes the transition alone, while the normal component flow remains laminar.

The behavior of the data above 1.955 K suggests that the normal fluid component may also become unstable above $\hat{U} \approx 100$. Indeed, the normal fluid fraction becomes significant at these temperatures, its kinematic viscosity $\nu_n = \eta/\rho_n$ decreases and the Donnelly number controlled instability in the normal fluid occurs at these higher temperatures earlier than the Donnelly-Glaberson type instability in the superfluid component. Mutual friction then tends to couple the normal and superfluid velocity fields together, until eventually He II (at quasiclassical scales) behaves as a single fluid possessing an effective kinematic viscosity. In the limit of very large velocities the drag ought to become velocity-independent, in the same fashion as in classical viscous fluids.

V. DISCUSSION

A. Two-fluid Regime

Let us generalize the described above experimental results on the two fluid He II flows due to several types

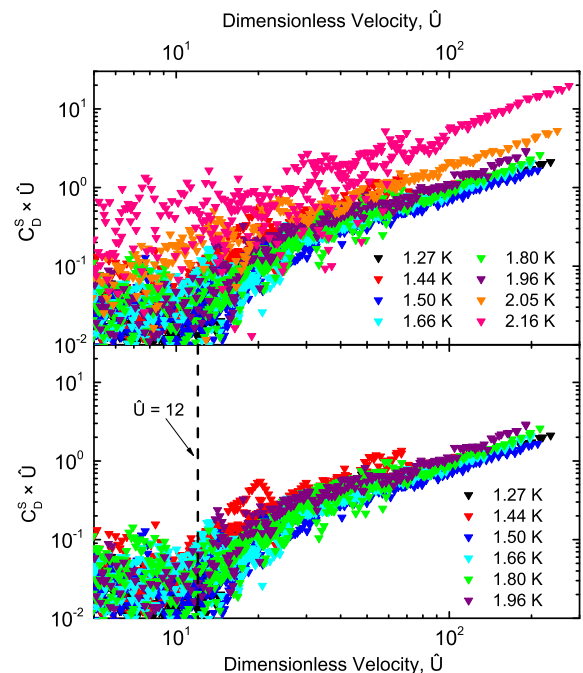


FIG. 14. Product of the disc's non-linear superfluid drag coefficient and dimensionless velocity as a function of the dimensionless velocity at various temperatures. Below about 1.955 K, the viscous drag acting on the disc collapses to a single dependence, but the instability is not described in terms of classical fluid dynamics as shown in the bottom panel.

of oscillators. In all of them the normal fluid flow is characterized by high Stokes number, and for low velocities it is laminar. In this limit the superflow is either (almost) potential or, in the case of torsionally oscillating disc, the superfluid component remains (almost) stationary in the laboratory frame of reference. Here almost means that there always exist remnant quantized vortices, whose density can be estimated based on the work of Awschalom, Milliken and Schwarz⁶⁹. We therefore have two (almost) independent velocity fields and flows of the normal and superfluid components can be treated independently.

It is therefore natural to treat, in this limit, the normal fluid as classical viscous fluid and not at all surprising that the drag coefficient C_D^s due to the normal fluid displays universal inverse scaling in terms of the Donnelly number Dn . Assuming that the superfluid component remains potential, upon increasing the Donnelly number the universal scaling holds and describes instabilities in the normal flow leading to gradual transition from laminar to turbulent drag regime in the normal flow. The normal fluid flow is no longer laminar and the overall He II flow can loosely be characterized as quantum turbulence, despite there are (almost) no quantized vortices in the flow. In some cases, the opposite situation appears in that the critical velocity associated with the Glaberson-Donnelly instability in the superfluid comes first, before

instability in the normal fluid flow. This situation is not new in superfluid hydrodynamics. Indeed, in experiments with superfluid $^3\text{He-B}$ the thick normal component virtually does not move in the laboratory frame of reference. Still, below about half of the critical temperature T_c the dissipative mutual friction coefficient falls below unity and a tangle of quantized vortices - superfluid turbulence - can exist in the soup of thick stationary normal fluid. In He II the situation is different in that the quantized vorticity coexists with the laminar boundary layer flow of the thin normal component. This situation is reported, to the best of our knowledge, for the first time and is best illustrated for the case of He II flow due to the torsionally oscillating discs at low temperatures (below about 1.9 K in this particular case).

Now, as the Donnelly-Glaberson instability occurs upon reaching a critical velocity, but the instability in the normal fluid flow is governed upon reaching a critical Donnelly number, a crossover is possible, thanks to the steep temperature dependence of the kinematic viscosity of the normal fluid. In other words, in our particular example of He II flow due to the torsionally oscillating disc, at high temperatures - closer to the superfluid transition temperature T_λ the classical instability in the normal fluid is reached first, while at low temperatures the situation is reversed in favor of the Donnelly-Glaberson instability. The existence of this crossover, observed also in the flow due to double-paddle oscillator, is reported for the first time and is quite remarkable. Either instability eventually serves as a trigger for the other one, mediated by the mutual friction force, until in the limit of high velocities, both fluids are tightly coupled in the vicinity of the oscillator and He II behaves as a single-component quasiclassical fluid.

B. Ballistic Regime and Scaling

In this Section, we demonstrate the applicability of the scaling laws derived for classical gases and the limits of their validity in superfluid helium. We plot the scaling function of the Weissenberg number $f(Wi)$ in Fig. 15 together with the experimental results obtained using a tuning fork both in the Newtonian hydrodynamic regime (this work) and in the ballistic regime³⁴. In the Newtonian regime (low Wi), we have included the flow enhancement and effective surface area in the analysis. The corresponding numeric factor $\alpha S_{\text{eff}}/S$ can be obtained from the dynamical similarity law $C_D^n = \Phi/Dn$ using $\alpha S_{\text{eff}}/S = 2\Phi A/S$. Apart from this, both asymptotics for $Wi \rightarrow 0$, and for $Wi \rightarrow \infty$ are practically identical. This important result means that a quasi-classical description of the excitation gas is feasible and accurate, provided that the mean free paths (or relaxation times) are calculated quantum-mechanically. We stress that the phonon drag extends to significantly higher Wi following the same asymptotic dependence, and for example at $T = 20$ mK, we have $Wi \simeq 5 \times 10^5$. At these tem-

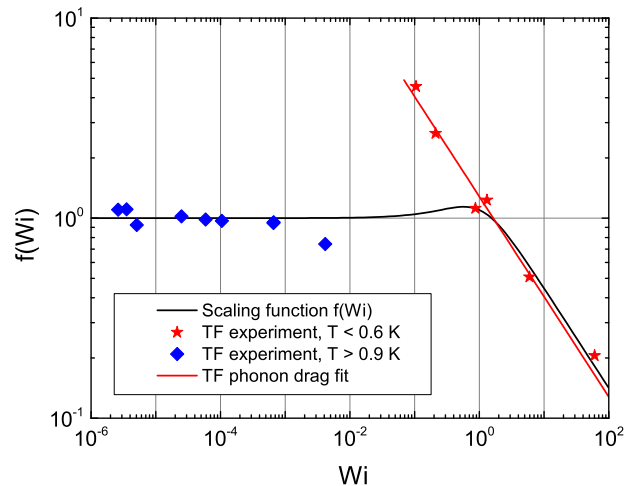


FIG. 15. Scaling function $f(Wi)$ as proposed in Ref. 1, compared with the results obtained in superfluid helium analysed using the theory outlined in Section IID. The low temperature data were obtained with the same tuning fork as discussed here and are adapted from our earlier work³⁴. They correspond to the temperature range between 0.3 K and 0.6 K. The solid straight line is a fit to the phonon drag observed in Ref. 34 using the form $1/Q_f \propto T^4$ and is the same for the fundamental mode and the overtone of the tuning fork. Lower temperatures are excluded due to the influence of intrinsic damping of the tuning fork. The data in the Newtonian regime correspond to temperatures between 0.9 K and 2.0 K, and have been corrected for the factor $\alpha S_{\text{eff}}/S$ obtained from the scaling of the normal component coefficient against the Donnelly number (see text). We note that we have assumed this factor to be exactly unity in the ballistic regime.

peratures, however, the dissipation of the tuning fork is dominated by intrinsic damping and it is difficult to extract the fluidic dissipation with good accuracy.

In the transitional regime, description of fluidic dissipation of an arbitrarily shaped oscillator is a considerable challenge in superfluid helium as well as in classical gases. Near the transitional regime, Fig. 15 shows significant deviation from the proposed scaling law and a number of issues need to be addressed to achieve a better understanding of the dissipative processes in the flow. For example, during the transition from the non-Newtonian regime to the Newtonian one, the influence of the detailed geometry of the oscillator must be in some way recovered. In He II, the situation is even more complicated, because the simple description of the phonon gas given above is no longer valid in the given range of temperatures. Instead, scattering processes involving rotons would need to be taken into account carefully, or possibly the entire dispersion relation $E = E(p)$ of excitations in He II would have to be described functionally and considered. The numerical calculations required to determine realistic relaxation times would be extremely demanding, but perhaps within the horizon of today's computational techniques. An approximative extension of the presented

description aiming to account for the transition regime is discussed in the jointly submitted Ref. 60 based on experimental data obtained with various different oscillators explored in the relevant temperature range.

VI. CONCLUSIONS

We have performed systematic measurements of high Stokes number flows of He II due to oscillatory motion of selected oscillators: vibrating wire resonator, tuning fork, double-paddle, and torsionally oscillating disc, over a broad temperature range where our working fluid, He II, displays the two-fluid behavior. We have shown that in this class of flow the origin of any instability in the normal or superfluid component can be determined by complex drag force analysis, based on which one can separate the drag offered to these oscillators by the normal and superfluid components of He II. For low velocities, we observe **universal viscous drag scaling** in terms of the suitably defined drag coefficient C_D^n and the normal fluid boundary-layer-based Reynolds number which we call the Donnelly number Dn .

The superfluid component does not contribute to the drag until an instability associated with extrinsic production of quantized vorticity occurs, governed by the dimensionless **velocity** $\hat{U} = U/\sqrt{\kappa\omega}$. The underlying physics involves Donnelly-Glaberson instability, i.e., self-reconnections of quantized vortices upon reaching a critical velocity. Until then the flow of the superfluid component is either potential (almost, excepting pinned remnant vortices) with the superfluid component playing a role of a physical vacuum, re-normalizing the hydrodynamic effective mass of the oscillators, or (in the case of the torsionally oscillating disc) the superfluid component remains stationary in the laboratory frame of reference.

Which instability (i.e., classical hydrodynamic instability of laminar flow of the normal component or Donnelly-Glaberson instability in the superfluid component) occurs first depends both on the geometry of the oscillator and temperature. We observe a crossover between these instabilities, thanks to the steep temperature dependence of the kinematic viscosity of the normal fluid. Upon increasing velocity, either instability can live on its own until eventually it serves as a trigger for the other one, mediated by the mutual friction force or by pressure forces. In the limit of high velocities, both fluids are tightly coupled in the vicinity of the oscillator and He II behaves as a single-component quasiclassical fluid.

Additionally, we have developed a formalism allowing direct comparison between measurements with resonators in He II and nanomechanical oscillators in classical dilute gases in both the Newtonian (hydrodynamic) and non-Newtonian (ballistic, free molecular) flow regimes. We have confirmed the universal scaling law suggested for high-frequency flows of classical gases by Ekinci, Yakhot, Rajauria, Colosquiac, and Karabacak¹ in a gas of massless quasiparticles – phonons

– and show that such a gas has the same asymptotic behavior, in spite of the significant differences in the underlying physics. These differences are manifest mainly in the fact, that we were required to invoke quantum mechanics for precise computation of mean free paths and relaxation times, and were required to use a relativistic-like fluid dynamical description of the phonon gas. The transitional flow regime remains an open challenge to theoretical, computational and experimental investigation and we have faith that our work will stimulate further research into this interesting and practically important issue.

ACKNOWLEDGMENTS

We thank E. Zemina and J. Luzuriaga for providing the data of Ref. 37 for further analysis. This research is funded by the Czech Science Foundation under project GAČR 17-03572S.

Appendix: Hydrodynamic Description of the Torsionally Oscillating Disc

Here we derive the equation of motion of the torsionally oscillating disc and the relevant hydrodynamic quantities. The motion of the harmonic torsional oscillator is given by the equation:

$$I_0 \ddot{\phi} + \kappa_f \phi = M_F, \quad (22)$$

where ϕ is the angular displacement, I_0 is the moment of inertia of the disc, κ_f is the moment of torsion of the fiber and M_F represents the moment of drag forces due to the surrounding fluid.

In laminar flow, with some simplification, the moment of the frictional forces can be calculated on the basis of the analytical solution of the Navier-Stokes equations. First, we assume that the velocity profile $\mathbf{u}(\mathbf{r}, t)$ locally corresponds to the rotation of the rigid body modulated with the distance from the disc, $\mathbf{u}(\mathbf{r}, t) = \boldsymbol{\Omega}(z, t) \times \mathbf{r}$, where $\boldsymbol{\Omega}(z, t) = (0, 0, \Omega(z, t))$, in which $\Omega(z, t)$ is the instantaneous angular velocity of the fluid at the distance z from the disk surface. Furthermore, we assume that the diameter of the disc $2R$ is significantly greater than its thickness h_d . The Navier-Stokes equation is then expressed in the form:

$$\frac{\partial \Omega(z, t)}{\partial t} = \nu \frac{\partial^2 \Omega(z, t)}{\partial z^2}, \quad (23)$$

where ν is the kinematic viscosity. The solution of this equation meeting the boundary conditions on the surface of the disc ($z = 0$) and at infinity has the form:

$$\Omega(z, t) = \Omega_0 e^{-z/\delta} e^{i(\omega t - z/\delta)}, \quad (24)$$

where Ω_0 is the instantaneous amplitude of the disc's angular velocity and $\delta = \sqrt{2\nu/\omega}$ is the viscous penetration depth.

The total torque acting on the disc will be determined by integration over both surfaces of the disc, neglecting the friction along its edge. The magnitude of the local viscous drag force F_v (per unit area) is given by $F_v(r, t) = \eta \partial u(z, t) / \partial z$, where η is the fluid dynamic viscosity. The magnitude of the local contribution to the torque of the viscous forces is then given as $M_v(r, t) = r F_v(r, t)$. The total moment of frictional forces is given as:

$$\begin{aligned} M_F(t) &= 2 \int_0^R \int_0^{2\pi} M_v(r, t) r d\theta dr \\ &= -\pi \eta \frac{1+i}{\sqrt{2}} \Omega_0 R^4 e^{i\omega t} \\ &= \frac{\pi}{\sqrt{2}} \frac{\eta \Omega_0 R^4}{(1-i)} \sqrt{\eta \omega \rho} \omega R^4 \phi_0 e^{i\omega t}. \end{aligned} \quad (25)$$

The moment of the friction forces is therefore phase-shifted with respect to the angular velocity of the disk by $\pi/4$. By defining a hydrodynamically induced moment of inertia $I_{HD} = \pi R^4 \sqrt{\eta \rho / 2 \omega}$ and the coefficient $\Gamma = \pi R^4 \sqrt{\eta \rho \omega / 2}$, we can rewrite the moment of the frictional forces as:

$$M_F(t) = -\Gamma \dot{\phi}(t) - I_{HD} \ddot{\phi}(t), \quad (26)$$

where the two terms on the right hand side correspond to dissipative and inertial forces, respectively.

The energy dissipated by the viscous forces can be obtained as:

$$\begin{aligned} \dot{E}(t) &= -2 \int_0^R \int_0^{2\pi} \text{Re}(M_v(r, t)) \text{Re}(\Omega_t) r d\theta dr \\ &= -\frac{\pi \eta \Omega_0^2 R^4}{\delta} [\sin(\omega t) \cos(\omega t) - \cos^2(\omega t)]. \end{aligned} \quad (27)$$

Averaging over one period, we get:

$$\langle \dot{E} \rangle = \frac{\pi}{2} \frac{\eta \Omega_0^2 R^4}{\delta}. \quad (28)$$

Using the fact that the total energy stored in the motion of the disc is $E = I_0 \Omega_0^2 / 2$, and its moment of inertia is given by $I_0 = m R^2 / 2$, we may define a fluidic quality factor:

$$\frac{1}{Q_f} = \frac{\langle \dot{E} \rangle}{\omega E} = \frac{A}{m_d} \sqrt{\frac{\eta \rho \omega}{2}}, \quad (29)$$

where $A = \pi R^2$ is the area of one side of the disc, and m_d is the disc's mass.

To define the drag coefficient, we follow the definition used in classical steady flow. The force F acting on a body in steady flow is given by $F = \frac{1}{2} C_D A' \rho U^2$, where C_D is the dimensionless drag coefficient, A' is the cross section of the body perpendicular to the direction of motion, ρ is the density of the fluid and U is the (homogeneous) velocity of the fluid. In analogy, it is possible to

define the drag coefficient for the torsionally oscillating disc from:

$$\frac{M_{FD}}{R} = \frac{1}{2} C_D A \rho \Omega_0^2 R^2, \quad (30)$$

where $M_{FD} = \Gamma \Omega_0$ is the dissipative part of the moment of frictional forces and we again use $A = \pi R^2$.

Finally, to define the dimensionless Donnelly number, we use the characteristic velocity at the circumference of the disc $U = R \Omega_0$, yielding:

$$\text{Dn} = \frac{R \Omega_0 \rho_n \delta_n}{\eta}. \quad (31)$$

Comparing with Eq. 30, we arrive at $C_D^n = 2/\text{Dn}$, where the normal component drag coefficient C_D^n differs from C_D only by replacing the density ρ with ρ_n .

Substituting 26 into the dynamic equation 22 and dividing by the total moment of inertia $I = I_0 + I_{HD}$ we get:

$$\ddot{\phi} + 2\gamma \dot{\phi} + \omega_0^2 \phi = 0, \quad (32)$$

where $\gamma = \Gamma/2I$ is the damping coefficient, and $\omega_0^2 = \kappa/I$ is the square of the intrinsic angular frequency of the undamped resonator. Thus, we have a standard equation of the damped harmonic oscillator, which is satisfied by the solution:

$$\phi(t) = \phi_0 e^{-\gamma t} e^{i\omega t}, \quad (33)$$

where the angular frequency ω is related to the frequency of a hypothetical undamped oscillator by $\omega^2 = \omega_0^2 - \gamma^2$.

After processing the recorded videos of the disc motion, we obtain data in the form of $\phi(t)$. From this, we determine the extrema $\phi_{0,i}$, and the logarithmic decrements $\alpha_i = \ln(\phi_{0,i-1}) - \ln(\phi_{0,i+1})$, which are related to the damping coefficient γ in Eq. 32 by $\gamma_i = \alpha_i \omega / (2\pi)$. The dissipative part of the moment of friction forces (the first term on the right hand side of Eq. 26) is then $M_{FD,i} = 2I\omega\gamma_i\phi_{0,i}$. The drag coefficient obtained from each experimental point may then be expressed as:

$$C_{D,i} = \frac{2I\alpha_i}{\pi A \rho R^3 \phi_{0,i}}. \quad (34)$$

If the hydrodynamic contribution to the moment of inertia is negligible, we may put $I \simeq I_0 = m R^2 / 2$, where the mass of the disc can be expressed as $m = A h_d \rho_d$, where h_d is the disc height and ρ_d its density. The drag coefficient can then be further simplified to:

$$C_{D,i} = \frac{1}{\pi} \frac{\rho_d h_d \alpha_i}{\rho R \phi_{0,i}}, \quad (35)$$

which no longer requires the precise knowledge of I or I_0 .

- ¹ K. L. Ekinci, V. Yakhot, S. Rajauria, C. Colosquiac and D. M. Karabacak, *Lab Chip* **10**, 3013 (2010).
- ² G. G. Stokes, *Transactions of the Cambridge Philosophical Society*, Vol. VIII. Part I, 105 (1843).
- ³ G. H. Keulegan, L. H. Carpenter, *J. of Research of the Natl. Bureau of Standards* **60**, 423 (1958).
- ⁴ Chang-Yi Wang, *J. Fluid Mech.* **32**, 55 (1968).
- ⁵ T. Sarpkaya, *J. Fluid Mech.*, **165**, 61 (1986).
- ⁶ M. Tatsuno, P. W. Bearman, *J. Fluid Mech.* **211**, 157 (1990).
- ⁷ K. L. Ekinci, D. M. Karabacak, and V. Yakhot, *Phys. Rev. Lett.* **101**, 264501 (2008).
- ⁸ E. C. Bullard, Jianchang Li, C. R. Lilley, P. Mulvaney, M. L. Roukes, and J. E. Sader, *Phys. Rev. Lett.* **112**, 015501 (2014).
- ⁹ M. Defoort, K. J. Lulla, T. Crozes, O. V. Maillet, O. Bourgeois, and E. Collin, *Phys. Rev. Lett.* **113**, 136101 (2014).
- ¹⁰ R. J. Donnelly and C. F. Barenghi, *J. Phys. Chem. Ref. Data* **27**, 1217 (1998).
- ¹¹ R. D. McCarty, *Thermophysical properties of helium-4 from 2 to 1500 K with pressures to 1000 atmospheres*, Technical Note 631, National Bureau of Standards, Gaithersburg, MD (1972).
- ¹² V. D. Arp and R. D. McCarty, *The properties of critical helium gas*, Technical Report, University of Oregon, Eugene, OR (1998).
- ¹³ S. Fuzier, B. Baudouy and S. W. Van Sciver, *Cryogenics* **41**, 453 (2001).
- ¹⁴ B. Saint-Michel, E. Herbert, J. Salort, C. Baudet, M. Bon Mardion, P. Bonnay, M. Bourgoïn, B. Castaing, L. Chevillard, F. Daviaud, P. Diribarne, B. Dubrulle, Y. Gagne, M. Gibert, A. Girard, B. Hébral, Th. Lehner, B. Rousset, and SHREK Collaboration, *Phys. Fluids* **26**, 125109 (2014).
- ¹⁵ J. J. Niemela, L. Skrbek, K. R. Sreenivasan, and R. J. Donnelly, *Nature* **404**, 837 (2000).
- ¹⁶ L. D. Landau, *J. Phys. (USSR)* **5**, 71 (1941); *J. Phys. (USSR)* **11**, 91 (1947).
- ¹⁷ R. J. Donnelly, *Quantized Vortices in Helium II* (Cambridge University Press, Cambridge, 1991).
- ¹⁸ C. F. Barenghi, L. Skrbek and K. R. Sreenivasan, *Proc. Natl. Acad. Sci. U.S.A.* **111**, 4647 (2014).
- ¹⁹ J. C. Wheatley, O. E. Vilches, and W. R. Abel, *J. Low Temp. Phys.* **4**, 1 (1968).
- ²⁰ A. C. Hollis-Hallett, *Proc. Roy. Soc. London. Series A*, **210**, 404 (1952).
- ²¹ R. J. Donnelly, A. C. Hollis-Hallett, *Annals of Phys.* **3**, 320 (1958).
- ²² E. L. Andronikashvili, *J. Phys. (Moscow)* **10**, 201 (1946).
- ²³ J. Jäger, B. Schuderer, and W. Schoepe, *Phys. Rev. Lett.* **74**, 566 (1995).
- ²⁴ M. Niemetz, W. Schoepe, *J. Low Temp. Phys.* **135**, 447 (2004).
- ²⁵ J. Luzuriaga, *J. Low Temp. Phys.* **108**, 267 (1997).
- ²⁶ S. I. Davis, P. C. Hendry, and P. V. E. McClintock, *Physica B* **280**, 43 (2000).
- ²⁷ H. A. Nichol, L. Skrbek, P. C. Hendry, P. V. E. McClintock, *Phys. Rev. Lett.* **92**, 244501 (2004).
- ²⁸ H. A. Nichol, L. Skrbek, P. C. Hendry, P. V. E. McClintock, *Phys. Rev. E* **70**, 056307 (2004).
- ²⁹ D. Charalambous, L. Skrbek, P. C. Hendry, P. V. E. McClintock, and W. F. Vinen, *Phys. Rev. E* **74**, 036307 (2006).
- ³⁰ P. Švančara, M. La Mantia, *J. Fluid Mech.*, **832**, 578 (2017).
- ³¹ R. Blaauwgeers, M. Blažková, M. Človečko, V. B. Eltsov, R. de Graaf, J. J. Hosio, M. Krusius, D. Schmoranz, W. Schoepe, L. Skrbek, P. Skyba, R. E. Solntsev, D. E. Zmeev, *J. Low Temp. Phys.* **146**, 537 (2007).
- ³² D. Garg, V. B. Efimov, M. Giltrow, P. V. E. McClintock, L. Skrbek, W. F. Vinen, *Phys. Rev. B* **85**, 144518 (2012).
- ³³ S. L. Ahlstrom, D. I. Bradley, M. Človečko, S. N. Fisher, A. M. Guénault, E. A. Guise, R. P. Haley, O. Kolosov, P. V. E. McClintock, G. R. Pickett, M. Poole, V. Tsepelin, and A. J. Woods, *Phys. Rev. B* **89**, 014515 (2014).
- ³⁴ D. Schmoranz, M. J. Jackson, V. Tsepelin, M. Poole, A. J. Woods, M. Človečko, and L. Skrbek, *Phys. Rev. B* **94**, 214503 (2016).
- ³⁵ E. N. Martinez, P. Esquinazi, J. Luzuriaga, *American J. of Physics* **58**, 1163 (1990).
- ³⁶ C. L. Spiel, R. O. Pohl, A. T. Zehnder, *Rev. Sci. Instrum.* **72**, 1482 (2001).
- ³⁷ E. Zemma and J. Luzuriaga, *J. Low Temp. Phys.* **166**, 171 (2012).
- ³⁸ D. Schmoranz, M. Jackson, E. Zemma and J. Luzuriaga, *J. Low Temp. Phys.* **187**, 482 (2017).
- ³⁹ D. Duda, P. Švančara, M. La Mantia, M. Rotter, L. Skrbek, *Phys. Rev. B* **92**, 064519 (2015).
- ⁴⁰ W. F. Vinen, *Proc. Roy. Soc. London. Series A*, **181**, 1524 (1961).
- ⁴¹ M. Morishita, T. Kuroda, A. Sawada, and T. Satoh, *J. Low Temp. Phys.*, **76**, 387 (1989).
- ⁴² D. I. Bradley, D. O. Clubb, S. N. Fisher, A. M. Guénault, R. P. Haley, C. J. Matthews, G. R. Pickett and K. L. Zaki, *J. Low Temp. Phys.* **138**, 493 (2005).
- ⁴³ R. Goto, S. Fujiyama, H. Yano, Y. Nago, N. Hashimoto, K. Obara, O. Ishikawa, M. Tsubota, and T. Hata, *Phys. Rev. Lett.* **100**, 045301 (2008).
- ⁴⁴ L. Skrbek and W. F. Vinen, *The use of vibrating structures in the study of quantum turbulence*, in *Progress in Low Temperature Physics* edited by M. Tsubota and W. P. Halperin (Elsevier, Amsterdam, 2009), Vol. XVI, Chap. 4.
- ⁴⁵ L. Skrbek and W. F. Vinen, *Proc. Natl. Acad. Sci. U.S.A.*, **111**, 4699 (2014).
- ⁴⁶ J. E. Sader, *J. Appl. Phys.* **84**, 64 (1998).
- ⁴⁷ W. I. Glaberson, W. W. Johnson and R. M. Ostermeier, *Phys. Rev. Lett.* **33**, 1197 (1974).
- ⁴⁸ R. Hänninen and W. Schoepe, *J. Low Temp. Phys.* **158**, 410 (2010).
- ⁴⁹ M. Blažková, D. Schmoranz, L. Skrbek, and W. F. Vinen, *Phys. Rev. B* **79**, 054522 (2009).
- ⁵⁰ D. Benin and H. J. Maris, *Phys. Rev. B* **18**, 3112 (1978).
- ⁵¹ D. S. Greywall, *Phys. Rev. B* **23**, 2152 (1981).
- ⁵² J. L. Yarnell, G. P. Arnold, P. J. Bendt, and E. C. Kerr, *Phys. Rev.* **113**, 1379 (1959).
- ⁵³ I. M. Khalatnikov, *An Introduction to the Theory of Superfluidity*, Westview Press, CO (2000).
- ⁵⁴ L. D. Landau, I. M. Khalatnikov, *Zh. Eksp. Teor. Fiz.* **19**, 637, 709 (1949), also *Collected Papers of L. D. Landau*, D. Ter Haar, ed. (Pergamon, Oxford, 1965), p. 494.
- ⁵⁵ L. D. Landau and E. M. Lifshitz, *Fluid Mechanics*, Perga-

- mon Press, London (1959).
- ⁵⁶ I. N. Adamenko, Yu. A. Kitsenko, K. E. Nemchenko, A. F. G. Wyatt, *Low Temp. Phys.* **35**, 198 (2009).
- ⁵⁷ H. J. Maris, *Phys. Rev. Lett.* **28**, 277 (1972), H. J. Maris, *Phys. Rev. A* **8**, 1980 (1973).
- ⁵⁸ D. Benin, *Phys. Rev. B* **11**, 145 (1975).
- ⁵⁹ A. A. Zadorozhko, G. A. Sheshin, E. Ya. Rudavskii, V. K. Chagovets, Yu. A. Kitsenko, *Fiz. Nizk. Temp.* **35**, 134 (2009).
- ⁶⁰ The manuscript jointly submitted to Phys. Rev. Letters.
- ⁶¹ D. I. Bradley, M. J. Fear, S. N. Fisher, A. M. Guenault, R. P. Haley, C. R. Lawson, P. V. E. McClintock, G. R. Pickett, R. Schanen, V. Tsepelin, L. A. Wheatland, *J. Low Temp. Phys.* **156**, 116 (2009).
- ⁶² D. Schmoranzner, M. La Mantia, G. Sheshin, I. Gritsenko, A. Zadorozhko, M. Rotter, L. Skrbek, *J. Low Temp. Phys.* **163**, 317-344 (2011).
- ⁶³ D. I. Bradley, M. Človečko, S. N. Fisher, D. Garg, E. Guise, R. P. Haley, O. Kolosov, G. R. Pickett, V. Tsepelin, D. Schmoranzner, and L. Skrbek, *Phys. Rev. B* **85**, 014501 (2012).
- ⁶⁴ A. M. Guénault, C. J. Kennedy, S. G. Mussett and G. R. Pickett, *J. Low Temp. Phys.* **62**, 511 (1986).
- ⁶⁵ K. J. Strnat, D. Li, and H. Mildrum, *High and Low Temperature Properties of Sintered Nd-Fe-B Magnets*, paper no. VIII-8 at the 8th Int. Workshop on Rare Earth Magnets and Their Applications, Dayton, OH, 6-8 May (1985); T. Hara, T. Tanaka, H. Kitamura, *et al.*, *Phys. Rev. Accel. Beams*, **7**, 050702 (2004).
- ⁶⁶ K. Karrai and R. D. Grober in *Near-Field Optics*, edited by M. A. Paesler and P. T. Moyer, *Proc. SPIE* **2535**, 69 (1995).
- ⁶⁷ S. Holt, P. Skyba, *Rev. Sci. Instrum.* **83**, 064703 (2012).
- ⁶⁸ D. I. Bradley, P. Crookston, M. J. Fear, S. N. Fisher, G. Foulds, D. Garg, A.M. Guénault, E. Guise, R. P. Haley, O. Kolosov, G. R. Pickett, R. Schanen and V. Tsepelin, *J. Low Temp. Phys.* **161**, 536 (2010).
- ⁶⁹ D. D. Awschalom, F. P. Milliken, and K. W. Schwarz, *Phys. Rev. Lett.* **53**, 1372 (1984).
- ⁷⁰ D. S. Hyman, M. O. Scully, A. Widom, *Phys. Rev.* **186**, 1 (1969).